Title

Validation of Finite-Element Models of Persistent-Current Effects in Nb_3Sn Accelerator Magnets

Journal

IEEE Transactions on Applied Superconductivity, 25(3)

ISSN

1051-8223

Authors

Wang, X
Ambrosio, G
Chlachidze, G
et al.

Publication Date

2015

DOI

10.1109/tasc.2014.2385932

Validation of Finite-Element Models of Persistent-Current Effects in Nb_3Sn Accelerator Magnets

X. Wang, G. Ambrosio, G. Chlachidze, E. W. Collings, D. R. Dietderich, J. DiMarco,
H. Felice, A. K. Ghosh, A. Godeke, S. A. Gourlay, M. Marchevsky, S. O. Prestemon,
G. Sabbi, M. D. Sumption, G. V. Velev, X. Xu, A. V. Zlobin

***Abstract*—Persistent magnetization currents are induced in superconducting filaments during the current ramping in magnets. The resulting perturbation to the design magnetic field leads to field quality degradation, in particular at low field where the effect is stronger relative to the main field. The effects observed in NbTi accelerator magnets were reproduced well with the critical-state model. However, this approach becomes less accurate for the calculation of the persistent-current effects observed in Nb_3Sn accelerator magnets. Here a finite-element method based on the measured strand magnetization is validated against three state-of-art Nb_3Sn accelerator magnets featuring different subelement diameters, critical currents, magnet designs and measurement temperatures. The temperature dependence of the persistent-current effects is reproduced. Based on the validated model, the impact of conductor design on the persistent-current effects is discussed. The performance, limitations and possible improvements of the approach are also discussed.**

***Index Terms*—Nb_3Sn accelerator magnets, field quality, magnetization.**

I. INTRODUCTION

SHIELDING currents are induced in the superconducting filaments during the magnetic field ramp in accelerator magnets. The resulted magnetization, of persistent nature, leads to field errors in the magnet aperture (persistent-current effects) that may degrade the accelerator performance in particular at low field, e.g., the injection level [1]. To understand and control the field errors induced by persistent currents, computational tools have been developed and successfully applied to NbTi accelerator magnets. These tools fall into two groups. The tools of Group 1, based on the critical-state model [2], calculate the strand magnetization with the field-dependent amplitude (critical current density $J_c(B)$) and profile of the shielding current in each superconducting filament [3]–[7]. Skipping the calculation of the strand magnetization, the tools of Group 2 use the measured strand magnetization either by directly assigning it to each individual strand [8] or by converting it to the nonlinear permeability of magnet coil [9]. Both groups achieve good agreement with the measurements from NbTi accelerator magnets. There are tools in each group considering the nonlinear iron saturation through the finite-element (FE) analysis [6], [7], [9].

High-J_c Nb_3Sn conductors are required for the next-generation accelerator magnets necessary for the luminosity and energy upgrade of the LHC [10]. Compared to NbTi, stronger magnetization effect is expected for Nb_3Sn conductors featuring larger filament (subelement) diameters and higher J_c. For example, the peak magnetization at 1.9 K, zero field of typical Restacked-Rod Processed (RRP) Nb_3Sn strands [11] with a subelement diameter of 50 μm is about 300 mT [12], [13], one order of magnitude higher than that of NbTi strands used in LHC with a filament diameter of 6 μm [14].

The self-field instability and flux jumps observed in high-J_c Nb_3Sn conductors at low field makes the initial application of the computational tools of Group 1 less powerful in reproducing the measurements performed on Nb_3Sn accelerator magnets [15]. To avoid this issue, an approach proposed earlier [16], [17], featuring the same principle as [9] and thus belonging to Group 2, is investigated here. It has been initially validated on NbTi [18] and successfully applied to Nb_3Sn accelerator magnets [19], [20]. We compare the measured and calculated field errors for state-of-art Nb_3Sn accelerator magnets and validate the calculation approach. With the calibrated model, we discuss the impact of conductor design on the persistent-current effects. The performance, limitations and possible improvements of the approach are discussed.

II. Nb_3Sn ACCELERATOR MAGNETS FOR MODEL VALIDATION

Three Nb_3Sn accelerator magnets are used to validate the calculation approach against a broad range of parameters relevant for the persistent-current effects. In addition to different conductor J_c and subelement diameters which directly contributes to magnetization effects, the magnets presented here feature two types (dipole and quadrupole), two design principles (shell and block) and two measurement temperatures

---

Manuscript received on August 27, 2014. The U.S. LHC Accelerator Research Program was supported through U.S. Department of Energy contracts DE-AC02-07CH11359, DE-AC02-98CH10886, DE-AC02-05CH11231, and DE-AC02-76SF00515. The HD program at LBNL was also supported by the U.S. Department of Energy with contract No. DE-AC02-05CH11231. The 11-T dipole program at FNAL was supported by the U.S. Department of Energy with contract No. DE-AC02-07CH11359. The work at the Ohio State University was supported by the DOE office of Science, Division of High Energy Physics, grant No. DE-SC0010312.

X. Wang, D. R. Dietderich, H. Felice, A. Godeke, S. A. Gourlay, M. Marchevsky, S. O. Prestemon, and G. Sabbi are with LBNL, Berkeley, CA 94720. (e-mail: xrwang@lbl.gov).

G. Ambrosio, G. Chlachidze, J. DiMarco, G. Velev and A. V. Zlobin are with FNAL, Batavia, IL 80510.

E. W. Collings, M. D. Sumption, and X. Xu are with OSU, Columbus, OH 43210.

A. K. Ghosh is with BNL, Upton, NY 11973.

(4.5 K and 1.9 K). The first magnet [Fig. 1(a)] is a block-type dipole developed at LBNL [21], [22]. Two conductor designs, 54/61 and 60/61, are used in the latest model, HD3b [23], [24]. HD3b was tested at 4.4 K and reached a bore field of 13.4 T, 86% of short-sample limit (SSL) [25].

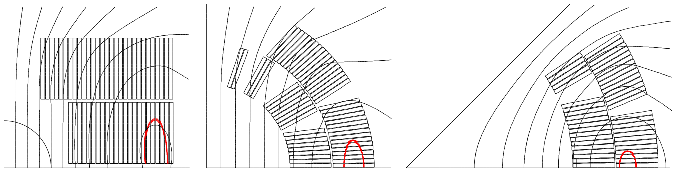

(a) (b) (c)

Fig. 1. Coil cross sections of three Nb_3Sn accelerator magnets and field lines. (a) HD3 at 14 kA (aperture: 40 mm). (b) MBHSP02 at 10 kA (aperture: 60 mm). (c) HQ02 at 14.6 kA (aperture: 120 mm). Also shown is a field boundary within which $|B|$ is less than 1.5 T at the quoted current.

The second magnet is MBHSP02 [Fig. 1(b)], an 11-T $\cos\theta$ dipole developed at FNAL for the High-Luminosity LHC (HL-LHC) [26]. The MBHSP02 magnet used a cored cable with RRP 150/169 Nb_3Sn conductor [27]. It was trained to $\sim 97\%$ of the magnet design field of 12 T [28] or $\sim 80\%$ of its SSL at 1.9 K.

The last one is HQ02 [Fig. 1(c)], a $\cos 2\theta$ quadrupole developed by the U.S. LHC Accelerator Research Program for the HL-LHC project [29]–[32]. HQ02 used a cored cable with RRP 108/127 conductor. In the recent test at 1.9 K, the magnet reached a gradient of 198 T/m, 95% of SSL [33], [34].

Table I summarizes the relevant magnet, strand and cable parameters for the calculation of persistent-current effects. As defined in [35], the subelement diameter is determined based on the strand diameter, Cu fraction, number of subelements and the assumption that each subelement has a circular cross section.

TABLE I
STRAND, CABLE AND MAGNET PARAMETERS. THE SELF-FIELD CORRECTED NON-CU J_C IS MEASURED FROM THE EXTRACTED STRANDS AT 12 T, 4.2 K.

Item	HD3b	HQ02	MBHSP02
Type	dipole	quad.	dipole
Design	block	$\cos 2\theta$	$\cos\theta$
Strand stack layout	54/61	108/127	150/169
Strand diameter (mm)	0.80	0.778	0.70
Subelement diameter (μm)	80	52	40
Non-Cu fraction (%)	54.4	45.5	48.2
Non-Cu J_c (A/mm^2)	3305	2961	2760
# of strands in cable	51	35	40
Cable packing factor (%)	83	83	88

III. PRINCIPLES OF FINITE-ELEMENT MODEL BASED ON STRAND MAGNETIZATION

In this section, we briefly review the calculation principles, the strand magnetization measurement and conversion procedures required for the calculation with the FE models. More details can be found in [9], [16], [17]. In a similar way that the nonlinear permeability of iron is introduced and treated in the finite-element magnetic models of accelerator magnets, the magnetization of a superconducting strand is modeled as the nonlinear permeability (or B-H property) of the coil region in the FE models.

The magnetic moment integrated over the entire sample volume can be measured with a vibrating sample magnetometer (VSM) [36]. The magnetization of HD and HQ strand samples (each about 4 mm long) was measured as a function of applied magnetic field with a commercial vibrating sample magnetometer (Quantum Design Model 6000) at the Ohio State University. Three consecutive ramps approximating to the magnetization state of a strand in a magnet are used: 1) the first up ramp to $H_{\max}$ after a zero-field cooling; 2) down ramp from $H_{\max}$ to zero field; and 3) the second up ramp to $H_{\max}$. Here $\mu_0 H_{\max}$ is 14 T at 1.9 K and 4.5 K. No significant ramp-rate dependence was observed for ramp rates ranging from 6 to 12 mT/s. Fig. 2 compares the magnetization of the strands used in three magnets.

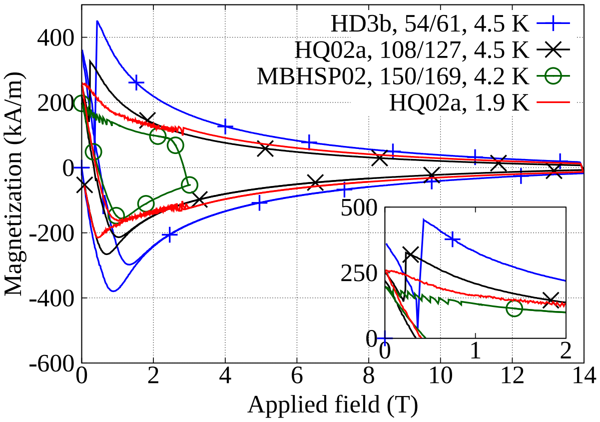

Fig. 2. Magnetization of the strands used in the magnets. The MBHSP02 strand data is from [27]. The inset shows the flux jumps when the applied field is below 1 T at 4.5 K and below 3 T for the 108/127 strand at 1.9 K.

Since individual cable is modeled in the FE model based on Opera 2D [37], the measured magnetization of a strand, $M(H)$, is translated to the $B(H)$ property of a cable according to $B(H) = \mu_0[H + \lambda M(H)]$, where λ is the cable packing factor (Table I). To take into account the magnetization hysteresis (Fig. 2), the $B(H)$ properties and persistent-current effects are calculated separately for each of the three ramp sequences. The magnetostatic problem is solved with nonlinear iterations until convergence is reached. The field errors during the down ramp and second up ramp are compared to the measurements. The geometric component is first removed from the calculated high-order multipoles which are then offset to match the measurements at high field.

IV. MEASUREMENT OF FIELD ERRORS INDUCED BY PERSISTENT CURRENTS

The field errors are measured with printed-circuit board coils rotating in the magnetic straight section [38]. The probe length is the same as the cable twist pitch length. To determine the field errors contributed by the persistent currents, a stair-step measurement is used. It starts with a current pre-cycle that sets the magnet into a reproducible magnetization state.

Following the pre-cycle, the current is ramped up and down in discrete intervals, leading to a stair-step profile. In order to differentiate the dynamic effect due to the inter-strand coupling currents (ISCC), at each step the current is held constant for 420 s for HD3b (without core) and 150 s for MBHSP02 and HQ02a (with core). The holding time is sufficient as the time constant for the exponential decay of the multipoles due to ISCC is 40–50 s for HD3b and 2–5 s for HQ02a [39].

The magnetic field in the aperture is expressed as a series expansion

$$B_y + iB_x = \sum_{n=1}^{\infty} (B_n + iA_n) \left(\frac{x+iy}{R_{\text{ref}}} \right)^{n-1}, \qquad (1)$$

where B_n are the normal and A_n are the skew multipole coefficients in Tesla at the reference radius R_{ref} [40]. The reference radius is 13 mm for HD, 17 mm for MBHSP02, and 40 mm for HQ. The normal and skew harmonics of order n normalized to the main field in units are obtained according to $b_n + ia_n = (B_n + iA_n)/B_m \times 10^4$. For dipole, $m = 1$ and $m = 2$ for a quadrupole. More details of the measurement protocol, experimental setup and data reduction can be found in [15], [41]–[43].

V. COMPARISON WITH MAGNET MEASUREMENTS

A. HD3b dipole at 4.4 K

Fig. 3 compares the measured and calculated transfer function and sextupole b_3. An offset of -3.5 units is applied to the calculated b_3 to match the measurement at high field. Since two conductors were used in the magnet, i.e., one coil has 54/61 conductors and the other has 60/61 conductors, three cases were calculated: 1) actual conductor configuration, 2) 60/61 conductors in both coils, and 3) 54/61 conductors in both coils.

Decay in the main field and b_3 due to the ISCC can be seen when the current is held constant. Multipole fluctuations related to flux jumps are also observed at low field.

B. MBHSP02 dipole at 4.5 K

Fig. 4 compares the measurement and calculation for MBHSP02. The calculation was performed based on the strand magnetization measured with the applied field up to 3 T at 4.2 K [27]. The calculated transfer function is offset by $+0.012$ T/kA to match the measurements up to 3 T. For b_3, an offset of $+8.44$ units due to the geometric effect is applied [41].

C. HQ02 quadrupole at 1.9 K and 4.5 K

Fig. 5 compares the main field transfer function at 1.9 K, and the b_6 at both 1.9 K and 4.5 K. The calculated b_6 is offset by $+1$ unit for both temperatures. The flux-jump induced multipole fluctuation can be seen below 6 kA during the up ramp at 4.5 K (Fig. 5(c)).

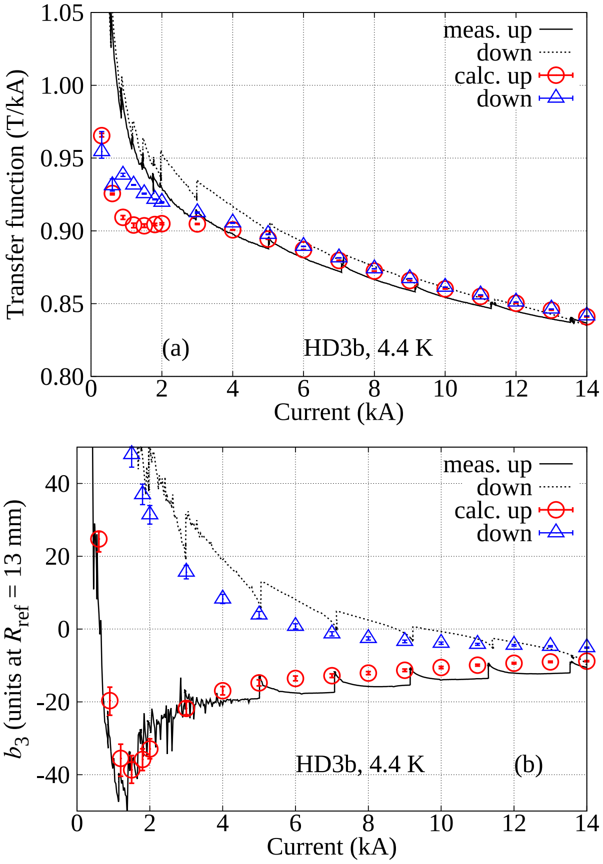

Fig. 3. HD3b at 4.4 K: measurement (lines) vs. calculation (symbols). (a) main field transfer function and (b) b_3. Three cases of the calculated persistent-current effects are shown here: 1) 54/61 and 60/61 conductors (symbols); 2) uniform 60/61 conductor (lower error bars); 3) uniform 54/61 conductors (upper error bars). $R_{\text{ref}} = 13$ mm.

VI. DISCUSSION

The persistent-current effects calculated by the FE models based on the measured strand magnetization agrees generally well with the measurements from three state-of-art high-field Nb$_3$Sn accelerator magnets. Together with the previously reported comparison [19], [20], the results presented here validates the FE approach. In this section, the temperature dependence of the persistent-current effects is discussed, followed by the impact of conductor design. The limitations and possible improvements of the model are discussed.

A. Temperature dependence of persistent-current effects

Comparing Fig. 5(b) and Fig. 5(c), one sees that the measured negative peak of b_6 increases from -29.4 units at 1.9 K to -33.1 units at 4.5 K. A similar temperature dependence of b_3 was observed in the 11-T dipole magnet [15], [41]. We attribute this behavior to the reduced strand magnetization at 1.9 K on the strand level due to the continuous flux jumps and the resulting J_c reduction when the applied field is below 3 T (Fig. 2). This behavior has been observed in high-J_c Nb$_3$Sn strands [12]. Above 3 T, with the absence of flux jump, higher J_c at 1.9 K leads to an increased magnetization and larger persistent-current effects. For example, the width of the hysteresis loop in b_6 at the same current between the up and

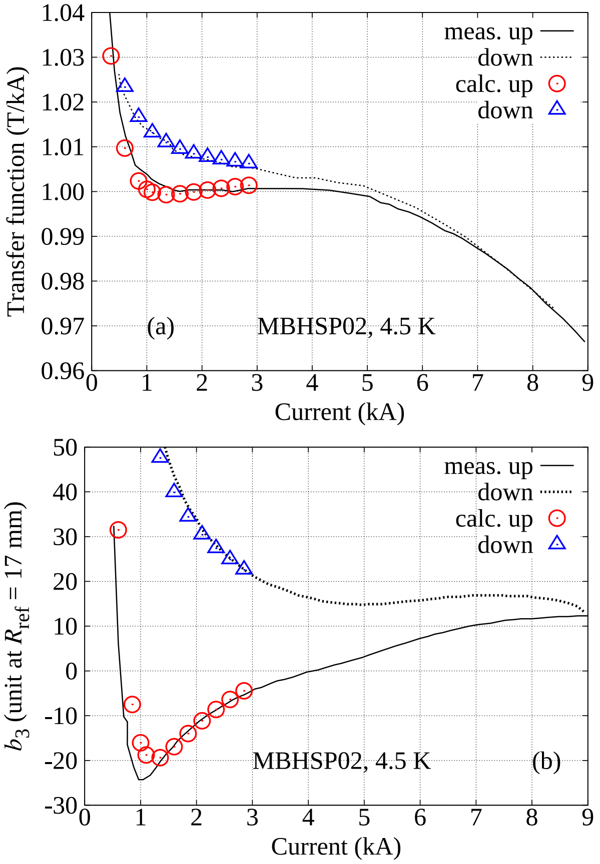

Fig. 4. The MBHSP02 dipole magnet at 4.5 K: measurement (lines) vs. calculation (symbols). (a) Main field transfer function and (b) b_3. The measured data is from [41]. $R_{\text{ref}} = 17$ mm.

down ramps, is about 11% to 33% larger at 1.9 K than those at 4.5 K for currents between 6 and 12 kA (Fig. 5). Since the temperature dependence is fully captured in the measured strand magnetization which is directly used in the FE models, the calculation reproduces the temperature dependence of the persistent-current effects observed in the measurements.

B. Impact of strand layouts

Larger number of subelements (smaller subelement diameter) reduces strand magnetization and improves strand stability. This has been demonstrated through the magnetization and transport measurements on single strands [11], [35]. Little is known, however, on how the reduced strand magnetization quantitatively impacts the persistent-current effects in magnets. With the validated FE model, we apply the magnetization data of three strands to the magnetic model of HD3 magnet to gain insight into this impact. The strands have the same diameter of 0.8 mm with an increasing number of subelements (Table II). The 108/127 conductor is from coil 5 of HQ01 magnet [44]. The 192/217 strand was developed by the U.S. HEP Conductor Development Program and heat treated at Brookhaven National Laboratory for a moderate J_c. The strand magnetization was measured at 1.9 K (Fig. 6).

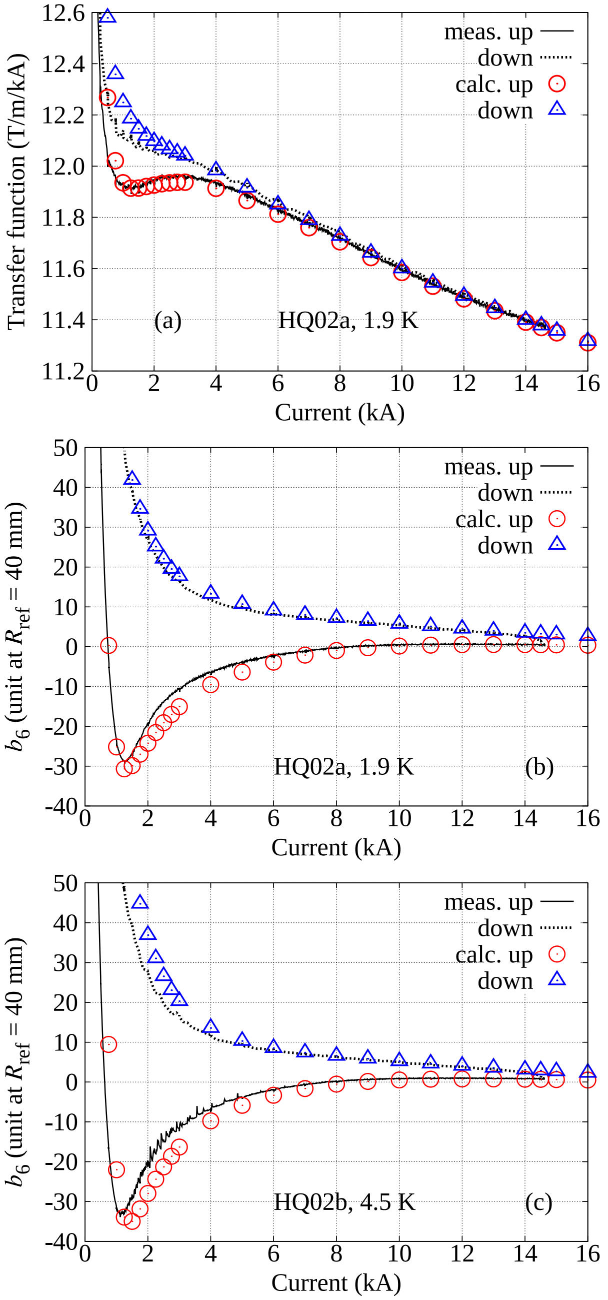

Fig. 5. The HQ02 quadrupole magnet: measurement (lines) vs. calculation (symbols). (a) main field transfer function at 1.9 K, (b) b_6 at 1.9 K and (c) b_6 at 4.5 K. $R_{\text{ref}} = 40$ mm.

TABLE II

STRANDS WITH INCREASING SUBELEMENT NUMBER. THE SELF-FIELD CORRECTED NON-CU J_{C} IS MEASURED AT 12 T, 4.2 K.

Strand stack layout	54/61	108/127	192/217
Non-Cu fraction (%)	54.4	46.1	49.0
Subelement diameter (μm)	80	52	40
Non-Cu J_c (A/mm^2)	3305	3084	2453

Fig. 7 compares the calculated b_3 induced by the persistent currents at 1.9 K for each strand. The cable packing factor is fixed at 83%. The contribution from the geometric and saturation effects is removed.

The negative peak of b_3 reduces from -25 units to -20 units by switching from 54/61 to 108/127 stack layout. The

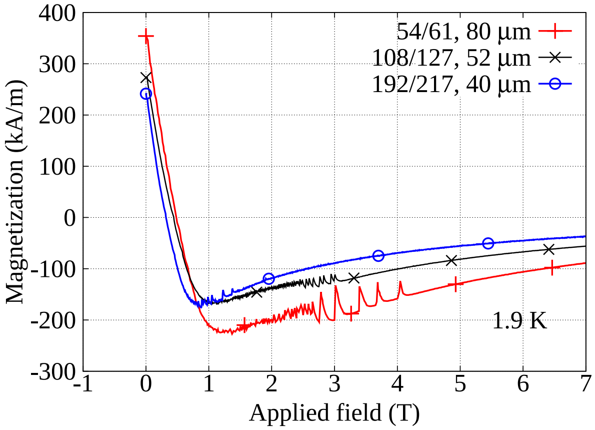

Fig. 6. Measured magnetization of three strands (Table II) at 1.9 K. Second up ramp. The flux jumps become less pronounced with increasing stack number in terms of amplitude and the field region where they appear.

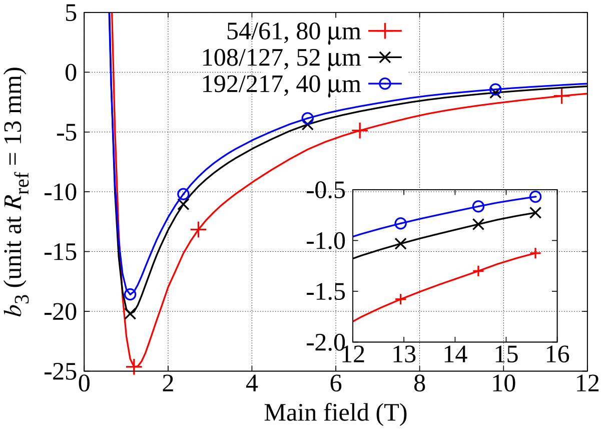

Fig. 7. Calculated b_3 induced by persistent currents of HD3b with different strand layouts at 1.9 K, second up ramp. The inset compares the b_3 at high field. $R_{\mathrm{ref}} = 13$ mm.

improvement is consistent with the 30% reduction in the measured strand magnetization above 1 T (Fig. 6). Further reduction in b_3 is negligible if switching from 108/127 to 192/217 layout. The difference in b_3 between these two layouts is less than 1.6 units above 1 T. Both smaller subelements and lower non-Cu J_c contribute to the reduced magnetization with the increasing stack number (Table II). While flux jumps become less pronounced with increasing stack number (Fig. 6), using conductors with a high stack number to limit the persistent-current effects comes at a cost of the decreased non-Cu J_c which limits the conductor transport capability and magnet performance margin. From this standpoint and considering that the field errors due to the persistent-current effects are still large for high-stack strand designs (Fig. 7), reducing the field errors with external correction schemes may be more desirable [17], [19], [45].

C. Strengths, limitations and possible improvements of the finite-element model

The FE models directly uses the measured strand magnetization and hence improves the calculation accuracy at low field compared to the existing approach based on the critical-state model. The validated model can be used for the prediction and correction of the persistent-current effects in high-field accelerator magnets. While the discussion here is focused on the RRP Nb_3Sn conductor, the method is expected to be compatible with its Powder-In-Tube counterpart and the high-T_c conductors (coated conductor and Bi-2212) that will contribute to the high-field accelerator magnets for future circular colliders [46].

Non-negligible discrepancies, however, still exists in particular at low fields where strands are not fully penetrated, e.g., the main field transfer function below 4 kA for HD3b [Fig. 3(a)]. These discrepancies can be attributed to the assumption that all regions of the magnet coil follow the same magnetization curve of the measured strand sample (section III). In fact, not all the strands are fully penetrated even at the nominal high field operation level. Fig. 1 shows the coil region where $|B|$ is less than 1.5 T, the minimum level from which, after the applied field decreases to zero, the following up ramp would follow the measurement of the single strand magnetization shown in Fig. 2. Thus, the magnetization curves for these non-fully-penetrated strands deviate from the measured curve, and contribute to the calculation error that is seen at low fields for the magnet cases studied here. To overcome this problem, a more flexible implementation of conductor permeability in the model is required. The cable magnetization scales directly from that of a single strand and the possible coupling of magnetization between strands is neglected. These limitations are less important at high field as J_c and the magnetization decrease with the applied field.

Another useful improvement is to consider the different reset currents where the second up ramp starts. The level of the reset current affects the persistent-current effect during the second up ramp at low field [15], [42]. The approach discussed here uses zero field as the minimum field for the magnetization measurements. This corresponds to the zero current in a magnet whereas the actual reset current was around 50 A during the tests. For a higher reset current, the approach must be modified to consider different initial fields in the strands. Accordingly, the strand magnetization should also be measured with different minimum field levels.

VII. CONCLUSION

The calculation of the persistent-current effects based on the direct application of the measured strand magnetization with finite-element models (Opera 2D) was validated against three state-of-art high-field Nb_3Sn accelerator magnets. The comparisons include two magnet types (dipole and quadrupole), two design principles (block and shell), and two test temperatures (1.9 K and 4.5 K). The RRP conductors used in the magnets range from the 54/61 layout with a subelement diameter of 80 μm to the 150/169 layout with a 40 μm subelement diameter. The calculated main-field transfer function and the first allowed harmonic agree reasonably well with the measurements of most magnet cases. The model reproduces the observed temperature dependence of the persistent-current effects. With the validated model, impact of strand design was quantified with 54/61, 108/127 and 192/217 layouts.

A 25%–35% reduction in b_3 from 54/61 to 108/127 layout is expected and further reduction from 108/127 to 192/217 layout is negligible. The strengths, limitations and possible improvements of this approach were discussed.

ACKNOWLEDGMENT

We thank the engineering and technical staff at BNL, FNAL, and LBNL for their dedicated contribution to the design, fabrication, and test of the model magnets that provide the valuable magnet data.

REFERENCES

[1] K.-H. Mess, P. Schmüser, and S. Wolff, *Superconducting accelerator magnets*. World Scientific, 1996, ch. 9.

[2] C. P. Bean, "Magnetization of hard superconductors," *Physical Review Letters*, vol. 8, pp. 250–253, Mar. 1962.

[3] M. A. Green, "Residual fields in superconducting magnets," in *Proceedings of the 4th International Conference on Magnet Technology*, BNL, Upton, NY, September 1972, pp. 339–346.

[4] H. Brück, R. Meinke, F. Müller *et al.*, "Field distortions from persistent currents in the superconducting HERA magnets," *Zeitschrift für Physik C Particles and Fields*, vol. 44, no. 3, pp. 385–392, 1989.

[5] K.-H. Mess, P. Schmüser, and S. Wolff, *Superconducting accelerator magnets*. World Scientific, 1996, ch. 6.

[6] C. Völlinger, M. Aleksa, and S. Russenschuck, "Calculation of persistent currents in superconducting magnets," *Phys. Rev. ST Accel. Beams*, vol. 3, p. 122402, Dec 2000.

[7] S. Russenschuck, *Field Computation for Accelerator Magnets: Analytical and Numerical Methods for Electromagnetic Design and Optimization*. Weinheim: John Wiley & Sons, 2010.

[8] R. Wolf, "Persistent currents in LHC magnets," *IEEE Transactions on Magnetics*, vol. 28, no. 1, pp. 374–377, 1992.

[9] S. Caspi, W. Gilbert, M. Helm *et al.*, "The effects of filament magnetization in superconducting magnets as calculated by Poisson," *IEEE Transactions on Magnetics*, vol. 23, no. 2, pp. 510–513, March 1987.

[10] L. Bottura, G. de Rijk, L. Rossi *et al.*, "Advanced accelerator magnets for upgrading the LHC," *IEEE Trans. Appl. Supercond.*, vol. 22, no. 3, p. 4002008, 2012.

[11] M. Field, Y. Zhang, H. Miao *et al.*, "Optimizing Nb_3Sn conductors for high field applications," *IEEE Trans. Appl. Supercond.*, vol. 24, no. 3, p. 6001105, June 2014.

[12] B. Bordini, D. Richter, P. Alknes *et al.*, "Magnetization measurements of high-J_c Nb_3Sn strands," *IEEE Trans. Appl. Supercond.*, vol. 23, no. 3, p. 7100806, June 2013.

[13] E. Collings, M. Susner, M. Sumption *et al.*, "Extracted strand magnetizations of an HQ type Nb_3Sn rutherford cable and estimation of transport corrections at operating and injection fields," *IEEE Trans. Appl. Supercond.*, vol. 24, no. 3, p. 4802605, June 2014, and references therein.

[14] L. Bottura and A. Godeke, "Superconducting materials and conductors: Fabrication and limiting parameters," *Reviews of Accelerator Science and Technology*, vol. 5, pp. 25–50, 2012.

[15] N. Andreev, G. Apollinari, B. Auchmann *et al.*, "Field quality measurements in a single-aperture 11 T demonstrator dipole for LHC upgrades," *IEEE Trans. Appl. Supercond.*, vol. 23, no. 3, p. 4001804, 2013.

[16] V. Kashikhin and A. Zlobin, "Calculation of coil magnetization effect in superconducting accelerator magnets," Fermi National Accelerator Laboratory, Tech. Rep. TD-00-010, February 2000.

[17] ——, "Correction of the persistent current effect in Nb_3Sn dipole magnets," *IEEE Trans. Appl. Supercond.*, vol. 11, no. 1, pp. 2058–2061, 2001.

[18] N. Andreev, T. Arkan, P. Bauer *et al.*, "Field quality of quadrupole R&D models for the LHC IR," in *Proceedings of Particle Accelerator Conference*, 1999, pp. 3194–3196.

[19] V. Kashikhin, E. Barzi, D. Chichili *et al.*, "Passive correction of the persistent current effect in Nb_3Sn accelerator magnets," *IEEE Trans. Appl. Supercond.*, vol. 13, no. 2, pp. 1270–1273, 2003.

[20] L. Chiesa, S. Caspi, D. Dietderich *et al.*, "Magnetic field measurements of the Nb_3Sn common coil dipole RD3c," in *Proceedings of the Particle Accelerator Conference.*, 2003, pp. 170–172.

[21] G. Sabbi, S. Bartlett, S. Caspi *et al.*, "Design of HD2: a 15 Tesla Nb_3Sn dipole with a 35 mm bore," *IEEE Trans. Appl. Supercond.*, vol. 15, no. 2, pp. 1128–1131, 2005.

[22] P. Ferracin, S. Bartlett, S. Caspi *et al.*, "Mechanical design of HD2, a 15 T Nb_3Sn dipole magnet with a 35 mm bore," *IEEE Trans. Appl. Supercond.*, vol. 16, no. 2, pp. 378–381, June 2006.

[23] H. Felice, F. Borgnolutti, S. Caspi *et al.*, "Challenges in the support structure design and assembly of HD3, a Nb_3Sn block-type dipole magnet," *IEEE Trans. Appl. Supercond.*, vol. 23, no. 3, p. 4001705, June 2013.

[24] D. Cheng, S. Caspi, D. Dietderich *et al.*, "Design and fabrication experience with Nb_3Sn block-type coils for high field accelerator dipoles," *IEEE Trans. Appl. Supercond.*, vol. 23, no. 3, p. 4002504, June 2013.

[25] M. Marchevsky, S. Caspi, D. Cheng *et al.*, "Test of the high-field Nb_3Sn dipole magnet HD3b," *IEEE Trans. Appl. Supercond.*, vol. 24, no. 3, p. 4002106, June 2014.

[26] A. V. Zlobin, N. Andreev, G. Apollinari *et al.*, "Development and test of a single-aperture 11 T Nb_3Sn demonstrator dipole for LHC upgrades," *IEEE Trans. Appl. Supercond.*, vol. 23, no. 3, p. 4000904, June 2013.

[27] E. Barzi, M. Bossert, G. Gallo *et al.*, "Studies of Nb_3Sn strands based on the Restacked-Rod Process for high-field accelerator magnets," *IEEE Trans. Appl. Supercond.*, vol. 22, no. 3, p. 6001405, 2012.

[28] A. V. Zlobin, N. Andreev, G. Apollinari *et al.*, "Quench performance of a 1 m long single-aperture 11 T Nb_3Sn dipole model for LHC upgrades," *IEEE Trans. Appl. Supercond.*, vol. 24, no. 3, p. 4000305, June 2014.

[29] H. Felice, G. Ambrosio, M. Anerella *et al.*, "Design of HQ – a high field large bore quadrupole magnet for LARP," *IEEE Trans. Appl. Supercond.*, vol. 19, no. 3, pp. 1235–1239, 2009.

[30] S. Caspi, G. Ambrosio, M. Anerella *et al.*, "Design of a 120 mm bore 15 T quadrupole for the LHC upgrade phase II," *IEEE Trans. Appl. Supercond.*, vol. 20, no. 3, pp. 144 –147, 2010.

[31] G. Sabbi, "Nb_3Sn IR quadrupoles for the high luminosity LHC," *IEEE Trans. Appl. Supercond.*, vol. 23, no. 3, p. 4000707, 2013.

[32] E. Todesco, H. Allain, G. Ambrosio *et al.*, "Design studies for the low-beta quadrupoles for the LHC luminosity upgrade," *IEEE Trans. Appl. Supercond.*, vol. 23, no. 3, p. 4002405, 2013.

[33] G. Chlachidze, G. Ambrosio, M. Anerella *et al.*, "Performance of HQ02, an optimized version of the 120 mm Nb_3Sn LARP quadrupole," *IEEE Trans. Appl. Supercond.*, vol. 24, no. 3, June 2014.

[34] H. Bajas, G. Ambrosio, M. Anerella *et al.*, "Test results of the LARP HQ02b magnet at 1.9 K," 2015, IEEE Trans. Appl. Supercond., to be published.

[35] L. Cooley, S. Chang, and A. Ghosh, "Magnetization, RRR and stability of Nb_3Sn strands with high sub-element number," *IEEE Trans. Appl. Supercond.*, vol. 17, no. 2, pp. 2706–2709, June 2007.

[36] S. Le Naour, L. Oberli, R. Wolf *et al.*, "Magnetization measurements on LHC superconducting strands," *IEEE Trans. Appl. Supercond.*, vol. 9, no. 2, pp. 1763–1766, June 1999.

[37] Cobham Technical Services, "Opera electromagnetics finite element software suite," http://operafea.com/.

[38] J. DiMarco, G. Chlachidze, A. Makulski *et al.*, "Application of PCB and FDM technologies to magnetic measurement probe system development," *IEEE Trans. Appl. Supercond.*, vol. 23, no. 3, p. 9000505, 2013.

[39] X. Wang, G. Ambrosio, F. Borgnolutti *et al.*, "Multipoles induced by inter-strand coupling currents in LARP Nb_3Sn quadrupoles," *IEEE Trans. Appl. Supercond.*, vol. 24, no. 3, p. 4002607, June 2014.

[40] A. K. Jain, "Basic theory of magnets," in *CERN Accelerator School: measurement and alignment of accelerator and detector magnets*, 1998, no. CERN-98-05, pp. 1–26.

[41] G. Chlachidze, J. DiMarco, N. Andreev *et al.*, "Field quality study of a 1-m-long single-aperture 11-T Nb_3Sn dipole model for LHC upgrades," *IEEE Trans. Appl. Supercond.*, vol. 24, no. 3, p. 4000905, June 2014.

[42] J. DiMarco, G. Ambrosio, M. Buehler *et al.*, "Field quality measurements of LARP Nb_3Sn magnet HQ02," *IEEE Trans. Appl. Supercond.*, vol. 24, no. 3, p. 4003905, 2014.

[43] L. Bottura, "Standard analysis procedures for field quality measurement of the LHC magnets — part I: harmonics," LHC/MTA, Tech. Rep. LHC-MTA-IN-97-007, 2001.

[44] A. Godeke, G. Chlachidze, D. R. Dietderich *et al.*, "A review of conductor performance for the LARP high-gradient quadrupole magnets," *Superconductor Science and Technology*, vol. 26, no. 9, p. 095015, 2013.

[45] E. Collings, M. D. Sumption, M. Susner *et al.*, "Coupling- and persistent-current magnetizations of Nb_3Sn Rutherford cables," *IEEE Trans. Appl. Supercond.*, vol. 20, no. 3, pp. 1387–1390, June 2010.

[46] G. Sabbi, L. Bottura, D. Cheng *et al.*, "Performance characteristics of Nb_3Sn block-coil dipoles for a 100 TeV hadron collider," 2015, IEEE Trans. Appl. Supercond., to be published.